SUPPLEMENTARY MATERIAL

Projected-Dipole Model For Quantum Plasmonics

Wei Yan,[1,2] Martijn Wubs,[1,2] and N. Asger Mortensen[1,2]
[1]Department of Photonics Engineering, Technical University of Denmark, DK-2800 Kgs. Lyngby, Denmark
[2]Center for Nanostructured Graphene, Technical University of Denmark, DK-2800 Kgs. Lyngby, Denmark

CONTENTS

1. Time-Dependent Density-Functional Theory Calculation 1
2. Derivation of Polarizability of Projected Dipole Layer 2
3. Polarizability of Projected Dipole Layer in Real Space 3
4. Equivalent Boundary Condition of Projected Dipole Layer 5
5. Green's Function Surface Integral Method 6
6. Local Approximation, Shortest Geodesic Approximation, and Full Geodesic Approximation 8
7. Computation Time and Accuracy 9
8. Gap Effects 9
  8.1. Electron-Hole Excitations 10
  8.2. Gap Permittivity 13
  8.3. Projected-Dipole Gap Model 13
9. Near-Field Properties 15
References 16

1. TIME-DEPENDENT DENSITY-FUNCTIONAL THEORY CALCULATION

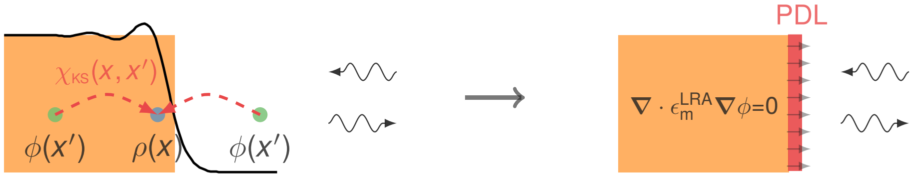

FIG. 1 (Left) Illustration of TDDFT computation of semi-infinite metal structure excited by an external electric field. The plasmonic response with quantum effects is described by the Kohn–Sham response function χ_{KS}. (Right) The quantum effects are equivalently represented in classical local-response electrodynamics by an infinitely thin layer of dipoles that point perpendicularly to the surface.

The time-dependent density-functional theory (TDDFT) computation routine of the free electron system can be found in Ref. 1. Here, we present the main equations and important terms of our TDDFT calculation for readers who may not be familiar with the TDDFT. Consider a semi-infinite metal system located at $x < 0$ driven by an electrostatic potential $\phi_{\mathrm{ext}} = \mathrm{e}^{\mathrm{i}\mathbf{k}_\parallel\cdot\mathbf{s}+k_\parallel x}$ in the linear regime, where $\mathbf{s} = y\hat{y} + z\hat{z}$, as illustrated in the left part of Fig. 1. We are interested in the reflected potential outside the metal region, which is denoted as $R_{\mathrm{ks}}\mathrm{e}^{\mathrm{i}\mathbf{k}_\parallel\cdot\mathbf{s}-k_\parallel x}$, where R_{KS} is the reflection coefficient. R_{KS} can be computed if knowing the induced electron density ρ with

$$R_{\mathrm{KS}} = -\frac{e}{2k_\parallel\epsilon_0}\int dx\rho(x)\mathrm{e}^{k_\parallel x}. \tag{1.1}$$

Employing TDDFT, ρ can be solved by

$$\rho(x)=\int dx'\ \left[\Xi(x,x',k_\parallel,\omega)\rho(x')-e\chi_{\mathrm{KS}}(x,x',k_\parallel,\omega)\phi_{\mathrm{ext}}(x')\right]. \tag{1.2}$$

Here χ_{KS} is the Kohn–Sham response function that is given by

$$\chi_{\mathrm{KS}}(x,x',k_\parallel,\omega) = \frac{2}{\pi^4}\int_0^\infty dq_1\int_0^\infty dq_2\int_{-\infty}^\infty\int_{-\infty}^\infty d\mathbf{q}_\parallel \frac{f_0(\epsilon_{q_2,\mathbf{q}_\parallel-\mathbf{k}_\parallel}) - f_0(\epsilon_{q_1,\mathbf{q}_\parallel})}{\hbar\omega - \epsilon_{q_1,\mathbf{q}_\parallel} + \epsilon_{q_2,\mathbf{q}_\parallel-\mathbf{k}_\parallel}}\psi^*_{q2}(x)\psi_{q1}(x)\psi^*_{q1}(x')\psi_{q2}(x'), \tag{1.3}$$

where $\epsilon_{q_1,\mathbf{q}_\parallel} = \hbar^2\left(q_1^2 + q_\parallel^2\right)/2m_\mathrm{e}$ represents the energy of a single Kohn-Sham orbital, and similarly for $\epsilon_{q_2,\mathbf{q}_\parallel-\mathbf{k}_\parallel}$; f_0 represents the Fermi–Dirac distribution function, which in the zero-temperature limit (adopted in our calculations) is simply $f_0 = 1$ for $\epsilon < \mathrm{E_F}$ and $f_0 = 0$ for $\epsilon > \mathrm{E_F}$ with $\mathrm{E_F}$ denoting the Fermi level of the system; $\psi_{\mathrm{q}_{1,2}}$ are the eigenfunctions of the Kohn–Sham orbitals, which asymptotically tend to $\sin(q_{1,2}x + \theta_{q_{1,2}})$ as $x \to -\infty$, and are computed using density-functional theory (DFT) [2]. Here, it is noted that the jellium approximation of the positive ion background is employed in the DFT and TDDFT computations. Further, Ξ is

$$\Xi(x, x', k_\parallel, \omega) = \int dx''\ \chi_{\mathrm{KS}}(x, x'', k_\parallel, \omega)\left[f_{\mathrm{Hartree}}(x'', x', k_\parallel) + f_{\mathrm{xc}}(x'', x')\right], \tag{1.4}$$

where f_{Hartree} and f_{xc} represent the Hartree and exchange-correlation (xc) kernels, respectively. f_{Hartree} and f_{xc} (adiabatical local-density approximation) are expressed as

$$f_{\mathrm{Hartree}}(x, x'', k_\parallel) = \frac{e^2}{2k_\parallel\epsilon_0}\mathrm{e}^{-k_\parallel|x-x''|}, \qquad f_{\mathrm{xc}}(x, x'') = \frac{dv_{\mathrm{xc}}^{\mathrm{HEG}}}{dn}\delta(x - x''), \tag{1.5}$$

where $v_{\mathrm{xc}}^{\mathrm{HEG}}$ represents the xc potential of a homogenous electron gas with a density of n, which here is chosen to be the Winger's xc potential [2].

2. DERIVATION OF POLARIZABILITY OF PROJECTED DIPOLE LAYER

Solving Eq. (1.2), we obtain the induced electron density ρ, and subsequently we find the reflection coefficient R_{KS} with Eq. (1.1). Next, we turn to the projected dipole layer (PDL) which consists of an infinitely thin dipole layer occupying the metal-air interface. Furthermore, the metal is described by its bulk permittivity $\epsilon_{\mathrm{m}}^{\mathrm{LRA}}$, see Fig. 1. To capture the quantum effects, we will by construction of the PDL ensure that the equivalent system reproduces the same reflection coefficient R_{KS} as we get from the TDDFT calculation. This leads to the unique value of the polarizability of the PDL denoted as α, as we explain in more detail in the following. The electric potentials in the air and metal regions can be expressed as

$$\phi_{\mathrm{air}} = \mathrm{e}^{k_\parallel x} + R_{\mathrm{KS}}(\omega, k_\parallel)\mathrm{e}^{-k_\parallel x}, \tag{2.1}$$

$$\phi_{\mathrm{metal}} = T_{\mathrm{KS}}\mathrm{e}^{k_\parallel x}, \tag{2.2}$$

They are naturally connected by boundary conditions. In particular, without the PDL, the boundary conditions are: (1) the continuity of the normal components of the displacement fields $\mathbf{D}$, i.e., $\partial\phi_{\mathrm{air}}/\partial x|_{x\to0^+} = \epsilon_{\mathrm{m}}^{\mathrm{LRA}}\partial\phi_{\mathrm{metal}}/\partial x|_{x\to0^-}$, and (2) the continuity of the parallel components of the electric fields, i.e, $\phi_{\mathrm{air}}|_{x\to0^+} = \phi_{\mathrm{metal}}|_{x\to0^-}$. With the PDL, the first boundary condition is maintained, while the second boundary condition undergoes a slight modification. As indicated in Sec. 4, the parallel component of the electric fields are discontinuous across the boundary with

$$\phi_{\mathrm{air}}|_{x\to0^+} - \phi_{\mathrm{metal}}|_{x\to0^-} = \frac{\mathrm{P_{PDL}}}{\epsilon_0} = -\alpha(\omega, k_\parallel)\frac{\partial\phi_{\mathrm{air}}}{\partial x}|_{x\to0^+}, \tag{2.3}$$

where $\mathrm{P_{PDL}}$ is the polarization moment of the PDL. With the two boundary conditions, we now have

$$1 - R_{\mathrm{KS}}(\omega, k_\parallel) = \epsilon_{\mathrm{m}}^{\mathrm{LRA}}(\omega)T_{\mathrm{KS}}(\omega, k_\parallel), \tag{2.4}$$

$$1 + R_{\mathrm{KS}}(\omega, k_\parallel) - T_{\mathrm{KS}}(\omega, k_\parallel) = -\alpha(\omega, k_\parallel)k_\parallel[1 - R_{\mathrm{KS}}(\omega, k_\parallel)]. \tag{2.5}$$

The two equations directly leads to the following expression for the polarizability:

$$\alpha(\omega, k_\parallel) = \frac{[1 - R_{\mathrm{KS}}(\omega, k_\parallel)] - \epsilon_m^{\mathrm{LRA}}[1 + R_{\mathrm{KS}}(\omega, k_\parallel)]}{k_\parallel\epsilon_m^{\mathrm{LRA}}(\omega)[1 - R_{\mathrm{KS}}(\omega, k_\parallel)]}, \tag{2.6}$$

which is Eq. (1) in the main text. In Fig. 2, we plot α for both Sodium and Aluminum.

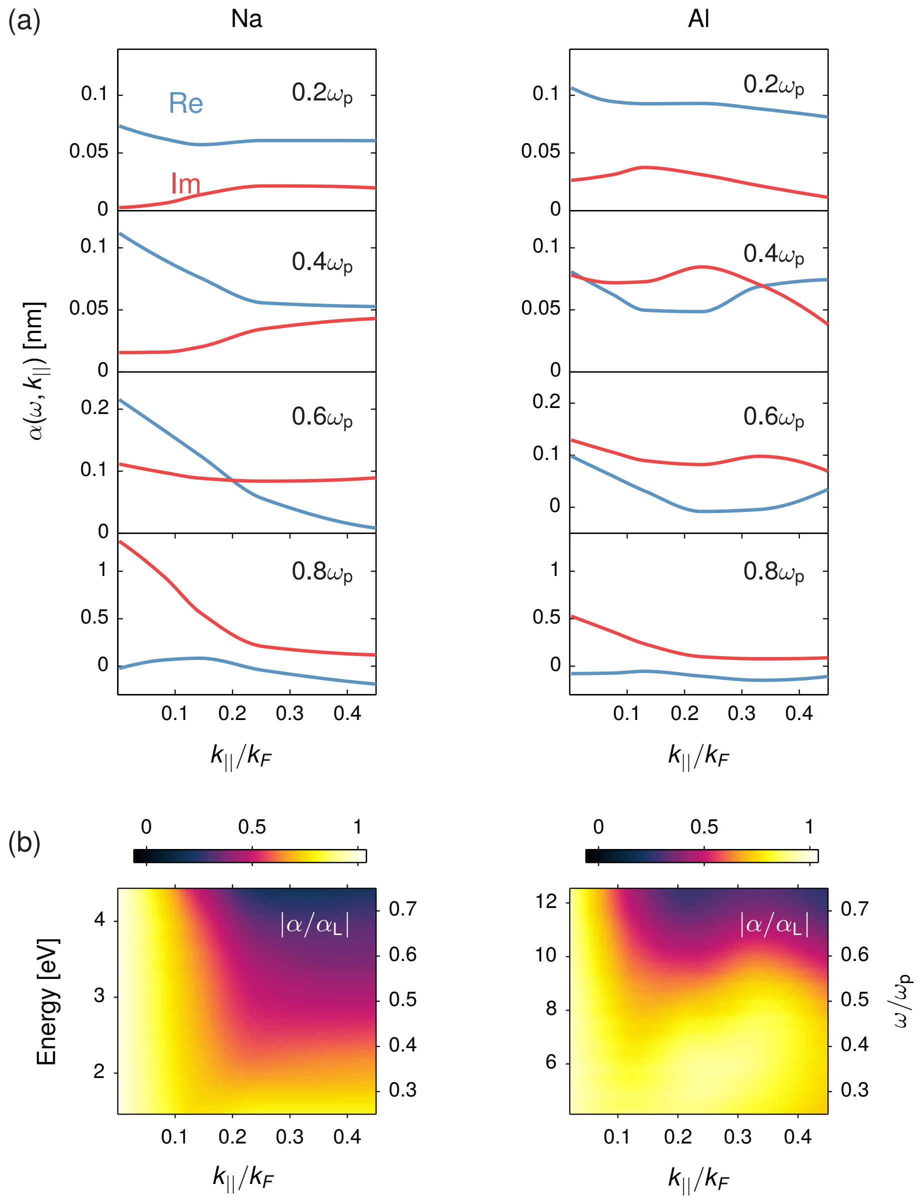

FIG. 2 (a) α, polarizability of the projected dipole layer for Sodium (left) and Aluminum (right) at different frequencies. (b) Amplitude of α normalized by its local limit approximation α_L for Sodium (left) and Aluminum (right).

3. POLARIZABILITY OF PROJECTED DIPOLE LAYER IN REAL SPACE

For the planar surface, the polarizability of the PDL in real space denoted as α_p is given by the inverse Fourier transform of α with

$$\begin{aligned}\alpha_\mathrm{p}(\omega, |\mathbf{s}-\mathbf{s}'|) &= \frac{1}{(2\pi)^2}\int_0^{2\pi} d\theta \int_0^{\infty} dk_{\parallel} k_{\parallel}\alpha(\omega, k_{\parallel}) e^{ik_{\parallel}|\mathbf{s}-\mathbf{s}'|\cos\theta}, \\ &= \frac{1}{2\pi}\int_0^{\infty} dk_{\parallel}\, k_{\parallel}\alpha(\omega, k_{\parallel}) J_0(k_{\parallel}|\mathbf{s}-\mathbf{s}'|). \end{aligned} \tag{3.1}$$

Here, J_0 represents the zeroth order of Bessel function. In Fig. 3, we plot α_p at frequencies $0.2\omega_\mathrm{p}$ and $0.8\omega_\mathrm{p}$ for Sodium and Aluminum. To evaluate α_p in Eq. (3.1) numerically, we set a cutoff to $k_{\parallel}$ at $0.45 \times 10^{10}\ \mathrm{m}^{-1}$. It is observed that α_p is confined like a Gaussian function with the half width at half maximum (HWHM) around 1 nm. Additionally, we see that the HWHM of α_p is larger at $0.8\omega_\mathrm{p}$ than at

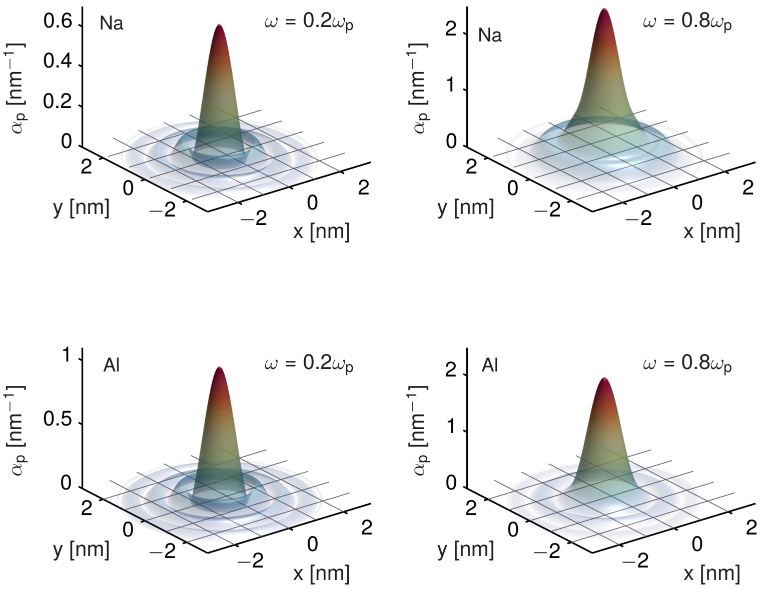

FIG. 3 The polarizability of the projected dipole layer in real space for Sodium and Aluminum at $\omega = 0.2\omega_{\mathrm{p}}$ and $\omega = 0.8\omega_{\mathrm{p}}$.

$0.2\omega_{\mathrm{p}}$, and is larger for Sodium than for Aluminium. These observations can be well understood from the $k_{\parallel}$ dependence of α shown in Fig. 2.

To generalize α_{p} of the planar surface to a curved surface for an arbitrary structure, we observe that the HWHM of α_{p} is around 1 nm. This indicates that, if the curved space appears as a flat one in the 1nm scale, α_{p} can be good approximation for the curved surface. Additionally, the distance $|s - s'|$ should be interpreted as the length of geodesic between two points, since the concept of geodesic is a direct generalization of the notion of a ”straight line” to ”curved spaces” [3]. Geodesics on a curved surface are illustrated in Fig. 4. It is seen that there is usually more than one geodesic, which can travel along the boundary clockwisely, anti-clockwisely, and also circularly. To define the generalized polarizability $\alpha(\omega, \mathbf{s}, \mathbf{s}')$ for a curved surface, we have the following options.

Full-Geodesic Approximation (FGA). Including the contributions of all geodesics for the mathematical completeness, there is

$$\alpha(\omega, \mathbf{s}, \mathbf{s}') = \sum_{g} \alpha_{\mathrm{p}}(\omega, |\mathbf{s} - \mathbf{s}'|_{g}), \tag{3.2}$$

where g runs over all geodesics between $\mathbf{s}$ and $\mathbf{s}'$, and $|\mathbf{s} - \mathbf{s}'|_{g}$ represents the length of the geodesic.

Shortest-Geodesic Approximation (SGA). Since α_{p} is a short-range function, the dominated contribution to Eq. (3.2) is from the term of the shortest path. Thus, we can make the SGA with

$$\alpha(\omega, \mathbf{s}, \mathbf{s}') = \alpha_{\mathrm{p}}(\omega, |\mathbf{s} - \mathbf{s}'|_{\mathrm{sg}}), \tag{3.3}$$

where $|\mathbf{s}-\mathbf{s}'|_{\mathrm{sg}}$ represents the length of the shortest geodesic. We note that Eq. (3.3) greatly simplifies Eq. (3.2). As demonstrated later, Eqs. (3.2) and (3.3) give almost the same numerical results for the structure size down to 2 nm, where the curvature does not spoil the validity of using α_{p} to construct the general polarizaiblity. Eq. (3.3) is Eq. (2) in the main text, which we use throughout the numerical examples in the main text.

Additionally, if we neglect the $k_{\parallel}$ dependence of α by replacing α with $\alpha_{\mathrm{L}} = \alpha(k = 0)$, Eqs. (3.2) and (3.3) can both be simplified to

Local Approximation.

$$\alpha_{(}\omega, \mathbf{s}, \mathbf{s}') = \alpha_{\mathrm{L}}\delta(\mathbf{s} - \mathbf{s}'). \tag{3.4}$$

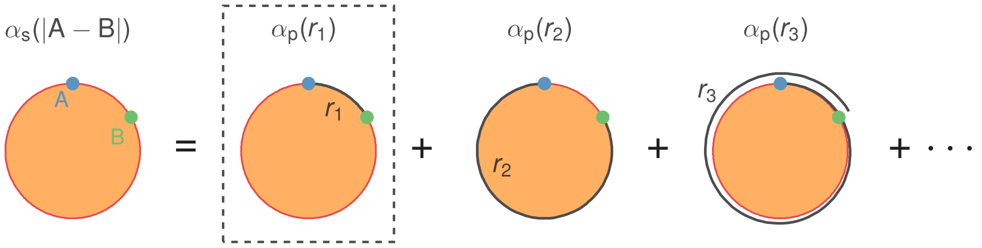

FIG. 4 Graphic illustrations of the full-geodesic approximation Eq. (3.2) that the polarizability of the projected dipole layer for a curved surface being the summation of the polarizability of the planner surface of the contributions from all geodesics. The first term on the right hand side of the equation surrounded by a dashed box indicates the contribution of the shortest geodesic, which gives the shortest-geodesic approximation Eq. (3.3).

> With this approximation, α_s becomes a local function, which will greatly simplify our numerics. However, such approximation is proper only when the large-$k_\parallel$ fields contribute insignificantly to the plasmon response.

Throughout our numerical examples we rely on Eq. (3.3), i.e., the shortest-geodesic approximation, due to its accuracy and simplicity. Accordingly, we need to know the length of the shortest path between two points on the PDL, i.e., $|\mathbf{s}-\mathbf{s}'|_{\text{sg}}$. For the 2D nanowire, the PDL boundary is a curve. The two points divide the boundary into two curves, and $|\mathbf{s}-\mathbf{s}'|_{\text{sg}}$ is simply the length of the shorter one. For an arbitrary 3D structure with a curved 2D surface, the finding of the shortest path on the curved surface can be done by well-developed numerical routines, such as the fast marching algorithm [4]. For a sphere, which we consider in the main text, $|\mathbf{s}-\mathbf{s}'|_{\text{sg}}$ can be evaluated analytically to give $|\mathbf{s}-\mathbf{s}'|_{\text{sg}} = r\theta(\boldsymbol{s},\boldsymbol{s}')$, where r is the radius of the sphere and $\theta(\boldsymbol{s},\boldsymbol{s}') \in [0 \;\; \pi]$ is the angle between two vectors $\boldsymbol{s}-\boldsymbol{o}$ and $\boldsymbol{s}'-\boldsymbol{o}$ with $\boldsymbol{o}$ being the origin of the sphere.

4. EQUIVALENT BOUNDARY CONDITION OF PROJECTED DIPOLE LAYER

The presence of the PDL is equivalent to the boundary condition (BC) as presented in the main text. The derivations are shown in this section. Consider the PDL with an arbitrary shape, and its unit vector of the surface normal is $\hat{\mathbf{n}}$ pointing toward the air background. The directly radiated electric fields from the PDL are

$$\mathbf{E}(\mathbf{r}) = \omega^2\mu_0 \int ds\; \mathbf{G}(\mathbf{r},\mathbf{s}) \cdot \mathrm{P}_{\text{PDL}}(\mathbf{s})\hat{\mathbf{n}}(\mathbf{s}), \tag{4.1}$$

where the dyadic Green's function $\mathbf{G}$ is

$$\mathbf{G}(\mathbf{r},\mathbf{r}') = \left[\mathbf{I} + \frac{1}{k^2}\nabla_{\mathbf{r}}\nabla_{\mathbf{r}}\right] g(\mathbf{r},\mathbf{r}'), \qquad g(\mathbf{r},\mathbf{r}') = \frac{\mathrm{e}^{\mathrm{i}k|\mathbf{r}-\mathbf{r}'|}}{4\pi|\mathbf{r}-\mathbf{r}'|}. \tag{4.2}$$

For $\mathbf{r} \notin \mathbf{s}$, employing the identity $\mathbf{E} = (\nabla \times \nabla \times \mathbf{E})/k^2$ and Eq. (4.1), we have

$$\mathbf{E}(\mathbf{r}) = \int ds\; \frac{1}{\epsilon_0} \nabla_{\mathbf{r}} g(\mathbf{r},\mathbf{s}) \times \left[\nabla_{\mathbf{s}} \times \mathrm{P}_{\text{PDL}}(\mathbf{s})\hat{\mathbf{n}}(\mathbf{s})\right]. \tag{4.3}$$

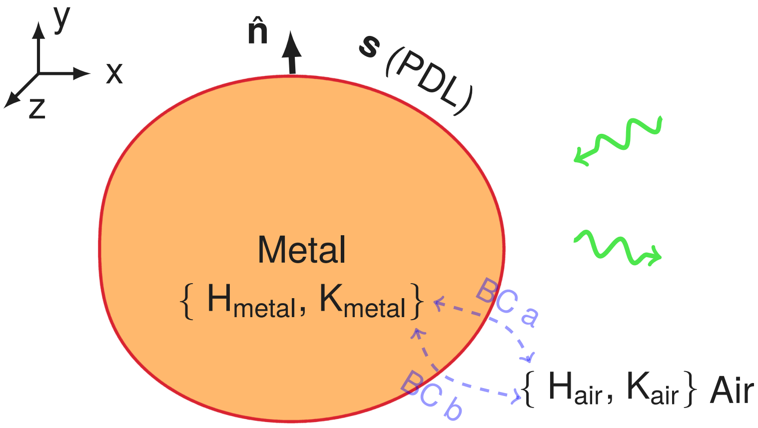

FIG. 5 Illustration of an electromagnetic wave interacting with a 2D nanowire surrounded by the PDL denoted as **s**. The fields $\{\mathrm{H}_{\mathrm{metal}}, \mathrm{K}_{\mathrm{metal}}\}$ in the nanowire and the fields $\{\mathrm{H}_{\mathrm{air}}, \mathrm{K}_{\mathrm{air}}\}$ relate each other through boundary condition (BC) a and b as defined in Section 5.

With Eq. (4.3), we wish to study the relation between the electric fields across the boundary **s**. For this, we evaluate

$$\begin{aligned}\lim_{\eta\to 0^+} \mathbf{E}\left[\mathbf{s}+\eta\hat{\mathbf{n}}(\mathbf{s})\right]-\mathbf{E}\left[\mathbf{s}-\eta\hat{\mathbf{n}}(\mathbf{s})\right] &= \lim_{\eta\to 0^+}\frac{1}{\epsilon_0}\int ds'\;\boldsymbol{\nabla}_{\mathbf{s}}\left(g\left[\mathbf{s}+\eta\hat{\mathbf{n}}(\mathbf{s}),\mathbf{s}'\right]-g\left[\mathbf{s}-\eta\hat{\mathbf{n}}(\mathbf{s}),\mathbf{s}'\right]\right)\times\left[\boldsymbol{\nabla}_{\mathbf{s}'}\times \mathrm{P}_{\mathrm{PDL}}(\mathbf{s}')\hat{\mathbf{n}}(\mathbf{s}')\right]\\ &= \lim_{\eta\to 0^+}\frac{1}{\epsilon_0}\int_{\mathbf{s}'\to\mathbf{s}} ds'\;\frac{-\eta\hat{\mathbf{n}}(\mathbf{s})}{2\pi\left(|\mathbf{s}-\mathbf{s}'|^2+\eta^2\right)^{3/2}}\times\left[\boldsymbol{\nabla}_{\mathbf{s}'}\times \mathrm{P}_{\mathrm{PDL}}(\mathbf{s}')\hat{\mathbf{n}}(\mathbf{s}')\right]\\ &= -\frac{1}{\epsilon_0}\hat{\mathbf{n}}(\mathbf{s})\times\left[\boldsymbol{\nabla}_{\mathbf{s}}\times \mathrm{P}_{\mathrm{PDL}}(\mathbf{s})\hat{\mathbf{n}}(\mathbf{s})\right]\\ &= -\frac{1}{\epsilon_0}\boldsymbol{\nabla}_{\mathbf{s}}\mathrm{P}_{\mathrm{PDL}}\left(\mathbf{s}\right),\\ &= -\boldsymbol{\nabla}_{\mathbf{s}}\int ds'\alpha(\omega,\mathbf{s},\mathbf{s}')\hat{\mathbf{n}}(\mathbf{s}')\cdot\mathbf{E}\left[\mathbf{s}'+\eta\hat{\mathbf{n}}(\mathbf{s}')\right]. \end{aligned} \tag{4.4}$$

where the second line is derived based on the observation that the term $\boldsymbol{\nabla}_{\mathbf{s}}\left[g(\mathbf{s}+\eta\hat{\mathbf{n}}_{\mathbf{s}},\mathbf{s}')-g(\mathbf{s}-\eta\hat{\mathbf{n}}_{\mathbf{s}},\mathbf{s}')\right]$ vanishes in the limit of $\eta\to 0$ except for $\mathbf{s}'$ near $\mathbf{s}$ denoted as $\mathbf{s}'\to\mathbf{s}$. Finally, we use the definition of the PDL in the last line. For the magnetic fields, following a similar routine, we find that

$$\lim_{\eta\to 0^+}\mathbf{H}\left[\mathbf{s}+\eta\hat{\mathbf{n}}(\mathbf{s})\right]-\mathbf{H}\left[\mathbf{s}-\eta\hat{\mathbf{n}}(\mathbf{s})\right]=0. \tag{4.5}$$

Eqs. (4.4) and (4.5) indicate that, in a numerical implementation, the contribution of the dipole layer is to induce a discontinuity of the parallel components (perpendicular with $\hat{\mathbf{n}}_{\mathbf{s}}$) across the PDL. Thus, we show that the presence of the PDL is equivalent to the boundary condition of the discontinuity of the parallel electric fields. In the electrostatic limit, we have $\mathbf{E}=-\nabla\phi$, which directly simplifies Eq. (4.4) to

$$\phi_{\mathrm{air}}(\mathbf{s})-\phi_{\mathrm{metal}}(\mathbf{s})=-\int ds'\alpha(\omega,\mathbf{s},\mathbf{s}')\hat{\mathbf{n}}(\mathbf{s}')\cdot\boldsymbol{\nabla}\phi_{\mathrm{air}}(\mathbf{s}'). \tag{4.6}$$

5. GREEN'S FUNCTION SURFACE INTEGRAL METHOD

With the equivalent BC for the PDL, the PDM can be conveniently adapted with well developed numerical techniques, such as the Green's function surface integral method (GSIM) [5] or the finite element method (FEM). Here, we choose the GSIM as the numerical tool, and focus on the 2D nanowire system with the cross section in the x–y plane incident by an electromagnetic wave with the electric field polarized in the same plane.

As a starting point, we consider the simple case that a single metallic nanowire imbedded in air/vacuum as illustrated in Fig. 5. The z-component magnetic fields in the nanowire and the background are denoted as $\mathrm{H}_{\mathrm{metal}}$ and $\mathrm{H}_{\mathrm{air}}$, respectively, which have the following integral representations

$$\mathrm{H}_{\mathrm{metal}}(\mathbf{r}) = \mathrm{H}^0_{\mathrm{metal}}(\mathbf{r}) - \int d\mathbf{s}\; G_{\mathrm{metal}}(\mathbf{r},\mathbf{s})\mathrm{K}_{\mathrm{metal}}(\mathbf{s}) + M_{\mathrm{metal}}(\mathbf{r},\mathbf{s})\mathrm{H}_{\mathrm{metal}}(\mathbf{s}), \tag{5.1a}$$

$$\mathrm{H}_{\mathrm{air}}(\mathbf{r}) = \mathrm{H}^0_{\mathrm{air}}(\mathbf{r}) + \int d\mathbf{s}\; G_{\mathrm{air}}(\mathbf{r},\mathbf{s})\mathrm{K}_{\mathrm{air}}(\mathbf{s}) + M_{\mathrm{air}}(\mathbf{r},\mathbf{s})\mathrm{H}_{\mathrm{air}}(\mathbf{s}). \tag{5.1b}$$

Here, $\mathrm{K}(\mathbf{s}) = \hat{\mathbf{n}}(\mathbf{s})\cdot\boldsymbol{\nabla}\mathrm{H}(\mathbf{s})$, and $M(\mathbf{r},\mathbf{s}) = \hat{\mathbf{n}}(\mathbf{s})\cdot\boldsymbol{\nabla}G(\mathbf{r},\mathbf{s})$. $\mathrm{H}^0_{\mathrm{metal}}$ and $\mathrm{H}^0_{\mathrm{air}}$ are the magnetic fields radiated by the sources in the nanowire and the background, respectively. G_{metal} and G_{air} are the scalar Green's functions of the nanowire and background, respectively, and they are

$$G_{\mathrm{metal}}(\mathbf{r},\mathbf{s}) = \frac{\mathrm{i}\mathrm{H}^{(1)}_0(k_{\mathrm{metal}}|\mathbf{r}-\mathbf{s}|)}{4}, \qquad G_{\mathrm{air}}(\mathbf{r},\mathbf{s}) = \frac{\mathrm{i}\mathrm{H}^{(1)}_0(k_{\mathrm{air}}|\mathbf{r}-\mathbf{s}|)}{4}, \tag{5.2}$$

with k_{metal} and k_{air} representing the wave numbers of the corresponding media. $\mathrm{H}^{(1)}_0$ is the zeroth-order Hankel function of the first kind. The fields $\{\mathrm{H}_{\mathrm{metal}}, \mathrm{K}_{\mathrm{metal}}\}$, and $\{\mathrm{H}_{\mathrm{air}}, \mathrm{K}_{\mathrm{air}}\}$ at the boundary determine the fields of the whole system, and need to be solved. For this, we require the boundary conditions to connect fields in different media

a. Continuity of the parallel magnetic fields:

$$\mathrm{H}_{\mathrm{metal}}(\mathbf{s}) = \mathrm{H}_{\mathrm{air}}(\mathbf{s}). \tag{5.3a}$$

b. Discontinuity of the parallel electric fields Eq. (4.4):

$$\frac{\mathrm{K}_{\mathrm{air}}(\mathbf{s})}{\epsilon_{\mathrm{air}}} - \frac{\mathrm{K}_{\mathrm{metal}}(\mathbf{s})}{\epsilon_{\mathrm{metal}}} = \boldsymbol{\nabla}_{\mathrm{s}}\cdot\int d\mathbf{s}'\alpha(\omega,\mathbf{s}-\mathbf{s}')\boldsymbol{\nabla}_{\mathbf{s}'}\mathrm{H}_{\mathrm{air}}(\mathbf{s}'), \tag{5.3b}$$

where $\epsilon_{\mathrm{metal}}$ and ϵ_{air} represent the permittivities of the nanowire and the air background.

Thus, the fields at the boundary can be determined with

$$\begin{aligned}
(1+M_{\mathrm{metal}})\mathrm{H}_{\mathrm{metal}} + G_{\mathrm{metal}}\mathrm{K}_{\mathrm{metal}} &= H^0_{\mathrm{metal}}, && (5.4a)\\
(1-M_{\mathrm{air}})\mathrm{H}_{\mathrm{air}} + G_{\mathrm{air}}\mathrm{K}_{\mathrm{air}} &= H^0_{\mathrm{air}}, && (5.4b)\\
\mathrm{H}_{\mathrm{metal}} &= \mathrm{H}_{\mathrm{air}}, && (5.4c)\\
\frac{\mathrm{K}_{\mathrm{air}}}{\epsilon_{\mathrm{air}}} - \frac{\mathrm{K}_{\mathrm{metal}}}{\epsilon_{\mathrm{metal}}} &= D_s\alpha D_s\mathrm{H}_{\mathrm{air}}, && (5.4d)
\end{aligned}$$

where matrix notation is adopted, and D_s is the matrix representation of $\boldsymbol{\nabla}_{\mathbf{s}}$. Here, it is noted that the singularities of $M_{\mathrm{metal}}(\mathbf{r},\mathbf{s})$ and $M_{\mathrm{air}}(\mathbf{r},\mathbf{s})$ as $\mathbf{r}\to\mathbf{s}$ contribute $\mp 1/2\delta(\mathbf{r}-\mathbf{s})$, respectively, to the integral equations.

Neglecting the retardation effects, i.e., in the electrostatic limit, we focus on the electric potentials instead of the magnetic fields. Accordingly, Eqs. (5.4a)-(5.4d) need a slight modification with

$$\begin{aligned}
(1+M)\phi_{\mathrm{metal}} + G\psi_{\mathrm{metal}} &= \phi^0_{\mathrm{metal}}, && (5.5a)\\
(1-M)\phi_{\mathrm{air}} + G\psi_{\mathrm{air}} &= \phi^0_{\mathrm{air}}, && (5.5b)\\
\epsilon_{\mathrm{metal}}\psi_{\mathrm{metal}} &= \epsilon_{\mathrm{air}}\psi_{\mathrm{air}}, && (5.5c)\\
\phi_{\mathrm{air}} - \phi_{\mathrm{metal}} &= -\alpha\psi_{\mathrm{air}}, && (5.5d)
\end{aligned}$$

where ϕ represents the electric potential, and $\psi = \hat{\mathbf{n}}\cdot\boldsymbol{\nabla}_{\mathbf{s}}\phi$; $G(\mathbf{r},\mathbf{s}) = -\ln(|\mathbf{r}-\mathbf{s}|)/2\pi$, and $M(\mathbf{r},\mathbf{s}) = \hat{\mathbf{n}}(\mathbf{s})\cdot\boldsymbol{\nabla}_{\mathbf{s}}G$. Similarl as in the case with retardation, the singularity of M as $\mathbf{r}\to\mathbf{s}$ contributes $\mp 1/2\delta(\mathbf{r}-\mathbf{s})$ to Eqs. (5.5a) and (5.5b), respectively. The above equations can be straightforwardly generalized to an arbitrary number of nanowires [5], and also to the three-dimensional (3D) case [6].

In the main text of the mansucript, the GSIM is employed to compute the plasmonic sturcutres for the PDM, and the agreements between the PDM and the TDDFT are shown. Here, we consider a dimer structure of two equilateral triangle nanowires excited by electric field polarized along the gap. The side length of the triangle is 24 nm with the vertex rounded by the circular arc with a 5.2 nm radius, and the gap between two nanowires is again 0.74 nm. The ploarizaiblity of the PDL is evaluated within

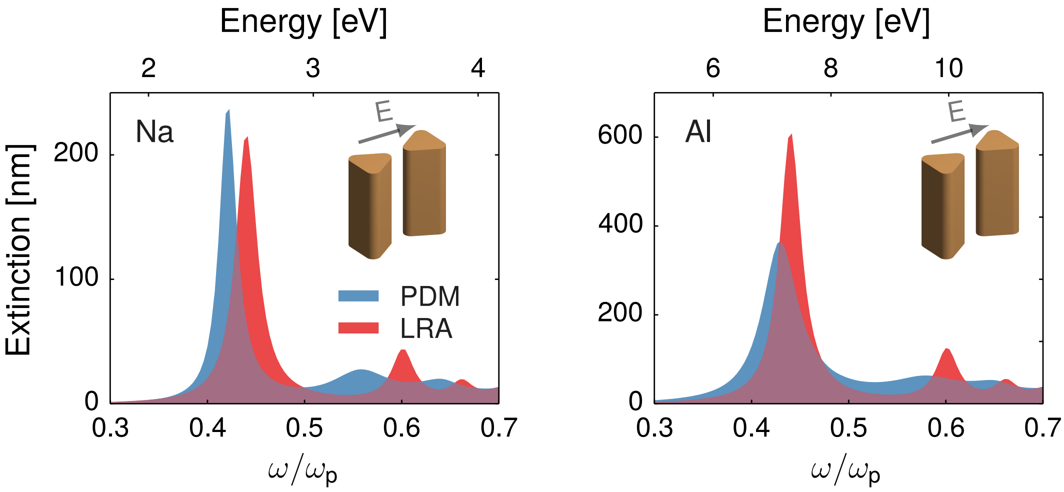

FIG. 6 Extinction cross section of the dimer structure of composed two equilateral triangle shaped nanowires for Sodium and Aluminum predicted by PDM and LRA in the electrostatic limit. The equilateral triangle has a side length of 24 nm with the vertex rounded by the circular arc with a 5.2 nm radius,, and the gap distance is 0.74 nm.

the shortest-geodesic approximation. The metal bulk permittivity is described by the Drude model $\epsilon_{\text{metal}}^{\text{LRA}} = 1 - \omega_p^2/\omega(\omega + i\gamma)$ with $\gamma = 0.027\omega_p$ for the LRA, and $\gamma = 0.014\omega_p$ for the PDM. The extinction cross sections for Sodium and Aluminum in the electrostatic limit are plotted in Fig. 6. By comparing the PDM and LRA results, we show that the quantum effects redshift the plasmon resonance frequency due to the spill-out, and also broaden the plasmon resonance width due to the electron-hole excitations near the surface. We notice that the the resonance broadening of Aluminum is wider than that of Sodium, which can be understood from Fig. 2 by comparing imaginary parts of α for Sodium and Aluminum.

6. LOCAL APPROXIMATION, SHORTEST GEODESIC APPROXIMATION, AND FULL GEODESIC APPROXIMATION

In Section 3, we introduce three level approximations for evaluating the real space ploarizability α of a curved surface. Here, we check their validity for predicting the plasmonic response. For brevity, we denote the PDM with the local approximation (LA) as $[\text{PDM}]^{\text{LA}}$, the PDM with the shortest geodesic approximation (SGA) as $[\text{PDM}]^{\text{SGA}}$, and the PDM with the full geodesic approximation as PDM^{FGA}.

Fig. 7 shows the extinction cross-section of the Sodium cylindrical wire with radius 4.9 nm and the corresponding dimer with gap distance 0.74 nm, comparing results for $[\text{PDM}]^{\text{LA}}$, $[\text{PDM}]^{\text{SGA}}$, $[\text{PDM}]^{\text{FGA}}$, LRA, TDDFT, and GNOR [7]. The single nanowire spectra of $[\text{PDM}]^{\text{LA}}$, $[\text{PDM}]^{\text{SGA}}$, $[\text{PDM}]^{\text{FGA}}$ show good agreements, and predict the surface plasmon (SP) resonance close to the TDDFT value, and redshifted with respect to the LRA. For the dimer case, the spectra of $[\text{PDM}]^{\text{SGA}}$, $[\text{PDM}]^{\text{FGA}}$, and TDDFT agree each other, but as expected not with $[\text{PDM}]^{\text{LRA}}$. The latter fact is due to the excitation of the high momentum-fields confined at the gap center, whose quantum effects are not well-captured by $[\text{PDM}]^{\text{LA}}$. The agreements between $[\text{PDM}]^{\text{SGA}}$ and $[\text{PDM}]^{\text{FGA}}$ indicate the dominant contribution to the PDL polarizability from the shortest geodesic. Additionally, we checked similar cases as above but with the cylinder radius down to 2 nm, and also find almost perfect agreements between $[\text{PDM}]^{\text{SGA}}$ and $[\text{PDM}]^{\text{FGA}}$. In the main text and the following, $[\text{PDM}]^{\text{SGA}}$ is employed, and is refereed to PDM for simplicity.

Remarks on GNOR. In Fig. 7, the results based on the GNOR are also included. Here, the GNOR includes the hydrodynamic nonlocal response and also the dissipative diffusion current as a means to qualitatively account for the surface scattering of the electrons. It is seen that the GNOR predicts the resonance blueshift with respect to the LRA results. While this is a common feature for noble metals, Sodium exhibits a redshift. Indeed, the blueshift in the GNOR results for Sodium contradicts the redshift that we observe with TDDFT and consequently also with the PDM. This is due to the neglect of the electron spill-out in the GNOR where electron confinement is treated in a hard-wall approximation. Thus, for Sodium and similar simple metals, where the electron spill-out effect is important, the GNOR is inappropriate [8; 9]. For the noble metals, for which the centroid of the induced charge at the plasmon

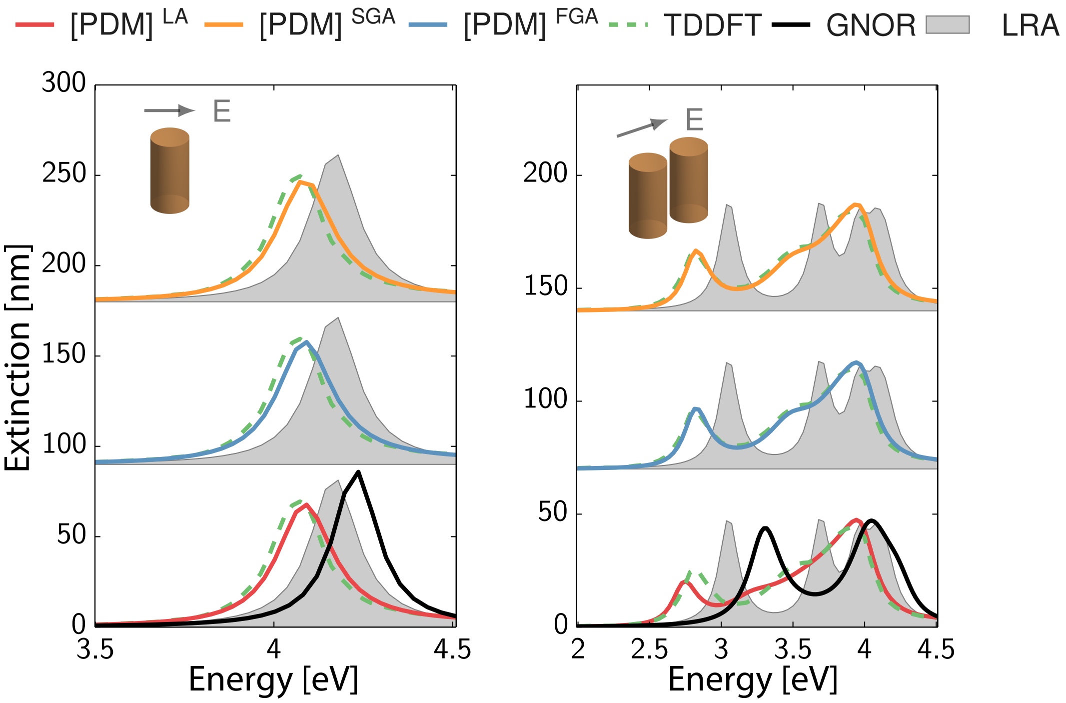

FIG. 7 Extinction properties of the Sodium cylindrical wire with radius 4.9 nm and the corresponding dimer with gap distance 0.74nm predicted $[\mathrm{PDM}]^{\mathrm{LA}}$, and $[\mathrm{PDM}]^{\mathrm{SGA}}$, and PDM. The TDDFT, LRA, and GNOR results are also included.

resonance resides inside the metal surface, the GNOR is on the other hand in a good agreement with the experimentally observed blueshift [10; 11].

7. COMPUTATION TIME AND ACCURACY

In Section 5, we show that the numerical computation of the PDM is similar to the approach used for the classical LRA, except for the modified boundary condition associated with the parallel electric field. This indicates that the computation of the PDM can be just as efficient as for the LRA. To illustrate this, we consider the example of a Sodium cylindrical dimer with radius 20 nm and gap 0.6 nm interacting with a uniform electric field along the gap. For our comparison we compute the extinction spectra. The probing frequency is chosen to be between 2 eV and 4.5 eV with 100 sampling points. In Fig. 8, we plot the mesh number of the boundary (in steps of 100) versus the run time, and also the mesh number versus the average relative error (ARE) for the LRA and PDM (within the shortest-geodesic approximation). The ARE at step n is defined as

$$\mathrm{ARE}(n) \equiv \frac{\sum_{i=1}^{N} \left[\sigma_n(\omega_i) - \sigma_{n-1}(\omega_i)\right] / \sigma_n(\omega_i)}{N}, \tag{7.1}$$

where σ represents the extinction cross section. It is observed that the computational behaviors of the LDA and PDM are qualitatively similar, even though the run time of the PDM is slightly longer than for the LRA.

8. GAP EFFECTS

The PDM considers the quantum effects of a single metal surface. For the dimer structure with a narrow gap, which supports interactions between two systems at quantum-wavefunction level, the gap effects are important, but not included in the PDM. To overcome this disadvantage, a simple way is to treat the gap as an effective medium with a permittivity characterizing the average electric response of the gap. The

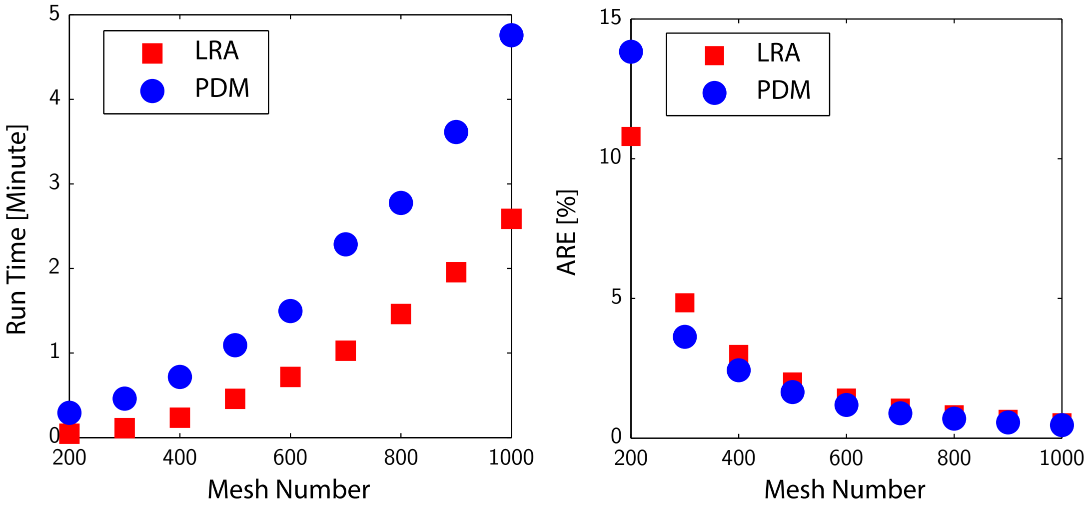

FIG. 8 Run time and the average relative error (for the extinction cross section) versus the mesh number for both the LRA and the PDM in the case of a e Sodium cylindrical dimer with radius 20 nm and gap 0.6 nm interacting with a uniform electric field along the gap.

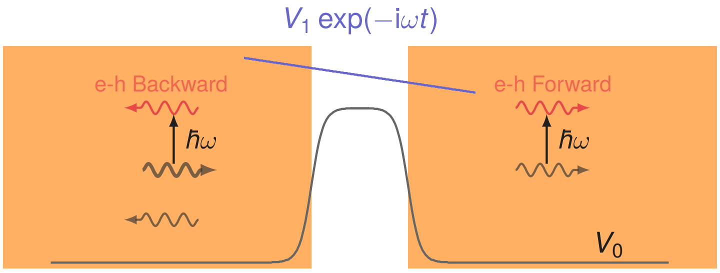

FIG. 9 Illustration of electron scattering by the gap between two metallic planar surfaces. Electron-hole excitations are permitted in both backward and forward directions. V_0 and V_1 exp($-$iωt) represent the ground state and external dynamic perturbative potential enegies, respectively.

approach was first introduced by the quantum corrected model (QCM) [12], which assumes that the gap permittivity holds a Drude form with the dissipation associated with a DC tunneling conductivity. The QCM has been successful in reproducing the gap phenomena numerically, such as the degeneration of the plasmon field enhancement and the emergence of the charge transfer plasmon. Its physical foundation that the quantum tunneling dominates the gap response is not justified, especially the tunneling concept is not well defined for the narrow gap case (below 3 Ångstrom for Sodium). Thus, to get the transparent understanding of the gap effects, in the main part of the paper, we offered an unambiguous extraction of the effective gap permittivity directly from TDDFT calculations, and extracted microscopic insights. Here, we present more technical details, and make some extended discussions.

8.1. Electron-Hole Excitations

When one investigates the electron response of a system, one basically looks for the real and imaginary parts of the permittivity. The latter relates with the loss, or more specifically with the electron-hole (e-h) excitations in our interested free electron system. It is therefore important to know how the gap participates in the e-h excitations. For this, we take the simple model of a vacuum gap formed between two parallel planar metal surfaces , as illustrated in Fig. 11. The excitation is a uniform electric field. Considering an electron state propagating from the left towards the gap junction seen in Fig. 11, the state will be scattered by the equilibrium (ground state) static potential denoted as V_0, and also obtain the chance to cause e-h excitations due to the dynamic perturbation V_1 exp($-$iωt). Basically, the e-h excitations can be divided into two types:

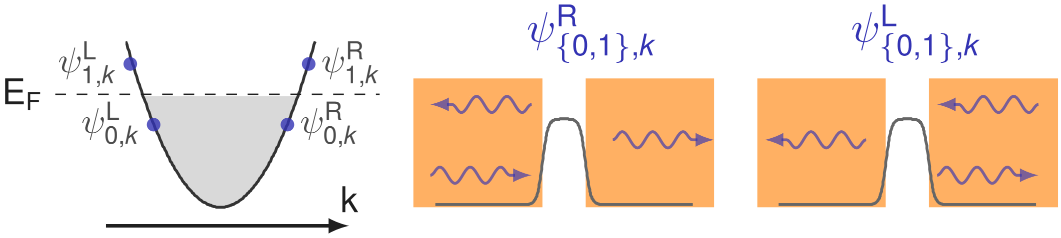

FIG. 10 Graphic illustration of notations $\psi^{\{\mathrm{L,R}\}}_{\{0,1\},k}$ used for extracting e-h backward and forward scatterings.

1. e-h backward scattering indicating that the excited electron state propagates in the opposite direction of the incident state.
2. e-h forward scattering indicating that the excited electron state propagates in the same direction of the incident state. In the large (relative to the work function scale) gap case, the e-h forward scattering includes the contribution from the QT if the dynamic energy $\hbar\omega$ is smaller than the work function, and also the photo-electric effect when $\hbar\omega$ is larger than the work function.

To quantitatively identify the contributions from the e-h backward and forward scatterings, we first introduce the notations $\psi^{\{\mathrm{L,R}\}}_{\{0,1\},k}$ for the Kohn–Sham orbitals with the physical meaning illustrated in Fig. 10. In particular, the subscripts ”0” and ”1” represent the states below and above the Fermi level, respectively, the subscript ”k” represents the wavenumber of the state inside the bulk, and the superscripts ”L” and ”R” represent the states propagating left and right, respectively. $\psi^{\{\mathrm{L,R}\}}_{\{0,1\},k}$ is normalized by

$$\left\langle \psi^{\mathrm{D}}_{i,k} | \psi^{\mathrm{D}'}_{i',k'} \right\rangle = \delta(k-k')\delta^{i'}_{i}\delta^{\mathrm{D}'}_{\mathrm{D}}, \tag{8.1}$$

where $i, i' \in \{0,1\}$, $\mathrm{D}, \mathrm{D}' \in \{\mathrm{L},\mathrm{R}\}$, and $\langle \mathrm{A}|\mathrm{B}\rangle \equiv \int_{-\infty}^{\infty} \mathrm{A}^*(\mathrm{x})\mathrm{B}(\mathrm{x})\mathrm{dx}$. We note that, in classical electrodynamics (excluding the exchange-correlation interactions), the dissipative power per unit area due to the induced current is given by

$$\mathrm{P_{disp}} = \frac{1}{2}\mathrm{Re}\,\langle E_1 | J_1 \rangle\,, \tag{8.2}$$

where E_1, J_1, represent the electric field, induced electron charge current, and induced electron density, respectively, and V^{sc}_1 represents the self-consistent electric potential energy including both the external incipient one $V_1\exp(-\mathrm{i}\omega\mathrm{t})$ and also the induced one from n_1. The second line of Eq. (8.2) is derived by using the charge conservation law and also integration by parts. Including the exchange-correlation effects within the TDDFT, Eq. (8.2) can be generalized by simply including the exchange-correlation potential in V^{sc}_1. Employing the linear response theory with the equilibrium Green's function technique [13], the microscopic expression of Eq. (8.2) is obtained

$$\begin{aligned}\mathrm{P_{disp}} =& \frac{m_e\omega}{8\pi\hbar^2}\int_{k_\mathrm{c}}^{k_\mathrm{F}} dk_0 \frac{k_\mathrm{F}^2-k_0^2}{k_1} \left[\underbrace{\left\langle\left(\psi^{\mathrm{R}}_{1,k_1}\right)^* |V^{\mathrm{sc}}_1|\psi^{\mathrm{R}}_{0,k_0}\right\rangle^2 + \left\langle\left(\psi^{\mathrm{L}}_{1,k_1}\right)^* |V^{\mathrm{sc}}_1|\psi^{\mathrm{L}}_{0,k_0}\right\rangle^2}_{\mathrm{e-h\ \ Backward}} + \underbrace{\left\langle\left(\psi^{\mathrm{R}}_{1,k_1}\right)^* |V^{\mathrm{sc}}_1|\psi^{\mathrm{L}}_{0,k_0}\right\rangle^2 + \left\langle\left(\psi^{\mathrm{L}}_{1,k_1}\right)^* |V^{\mathrm{sc}}_1|\psi^{\mathrm{R}}_{0,k_0}\right\rangle^2}_{\mathrm{e-h\ \ Forward}}\right] \\ &+ \frac{m_e\omega}{8\pi\hbar^2}\int_{0}^{k_c} dk_0 \frac{k_1^2-k_0^2}{k_1} \left[\underbrace{\left\langle\left(\psi^{\mathrm{R}}_{1,k_1}\right)^* |V^{\mathrm{sc}}_1|\psi^{\mathrm{R}}_{0,k_0}\right\rangle^2 + \left\langle\left(\psi^{\mathrm{L}}_{1,k_1}\right)^* |V^{\mathrm{sc}}_1|\psi^{\mathrm{L}}_{0,k_0}\right\rangle^2}_{\mathrm{e-h\ \ Backward}} + \underbrace{\left\langle\left(\psi^{\mathrm{R}}_{1,k_1}\right)^* |V^{\mathrm{sc}}_1|\psi^{\mathrm{L}}_{0,k_0}\right\rangle^2 + \left\langle\left(\psi^{\mathrm{L}}_{1,k_1}\right)^* |V^{\mathrm{sc}}_1|\psi^{\mathrm{R}}_{0,k_0}\right\rangle^2}_{\mathrm{e-h\ \ Forward}}\right]\end{aligned} \tag{8.3}$$

where k_c is defined by $\hbar^2k_\mathrm{c}^2/2m_\mathrm{e}+\hbar\omega = \mathrm{E_F}$, and k_1 relates to k_0 by $\hbar^2k_1^2/2m_\mathrm{e} = \hbar^2k_0^2/2m_\mathrm{e}+\hbar\omega$. In Eq. (8.3), the backward and forward scattering contributions are split in a manner to make the corresponding terms agreeing with the far field (deep inside the bulk metal) amplitudes of the backward and forward excited states. In the limiting case of an infinitely large gap, Eq. (8.3) just describes the e-h excitations of the single interface.

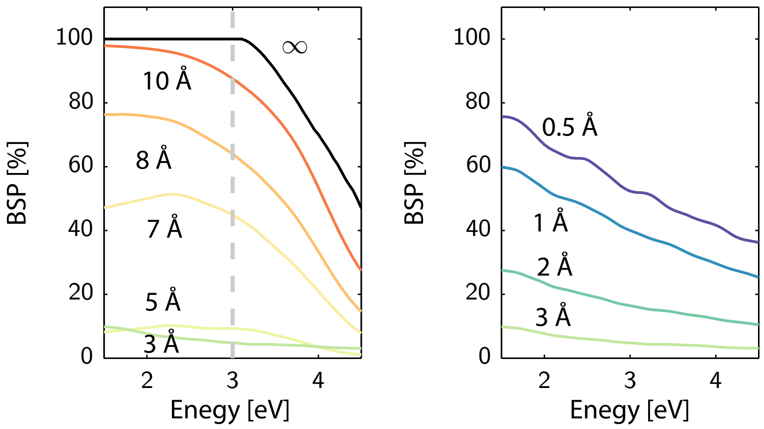

FIG. 11 Backward scattering proportion for two parallel planer Sodium interfaces with a varying vacuum gap.

Considering Sodium, we plot the backward scattering proportion (BSP), and also the forward scattering proportion (FSP) for different gap distances in Fig. 11. The results in Fig. 11 demonstrates the complicated behaviors of the gap related e-h excitations, and suggest the necessity of the full TDDFT extraction of gap permittivity, which we discuss in the main part of the paper.

The QCM attributes the total e-h excitations to the QT. With the implications of Fig. 11, we conclude that the QCM gives a qualitatively correct account for the damping under the following conditions: (1) the gap distance is in the range of 3-5 Å, where the backward scattering becomes relatively small and (2) the energy is smaller than the work function associated with an insolated interface (3.06 eV for the Sodium interface), since the high energy belongs to the regime of the photo-electric effect. However, the QCM is only qualitatively correct as the assumed Drude form conflicts the detailed dynamics of the gap as we have unraveled by TDDFT as seen in Fig. 13. For the gap distance below 3 Å, the tunneling picture is not physically sound, and the back scattering turns to increase. As a result, the response turns Drude-like, which is accidentally the character of the QCM too. In this regime, the emergence of the charge transfer plasmon is simply a manifestation of the vacuum gap to a Drude-like conductive gap due to the spill-out of the equilibrium electron density, and the e-h excitations are simply due to the scattering of the electron with the impurity of the junction. We believe that our new insight from TDDFT solves the controversy of the QCM; it gives reasonable numerical results because (1) the Drude permittivity becomes valid, (2) the dissipation in this regime is included by the interpolation of the large gap dissipation with choosing a physical limiting value that the damping approaches zero as the gap vanishes [12].

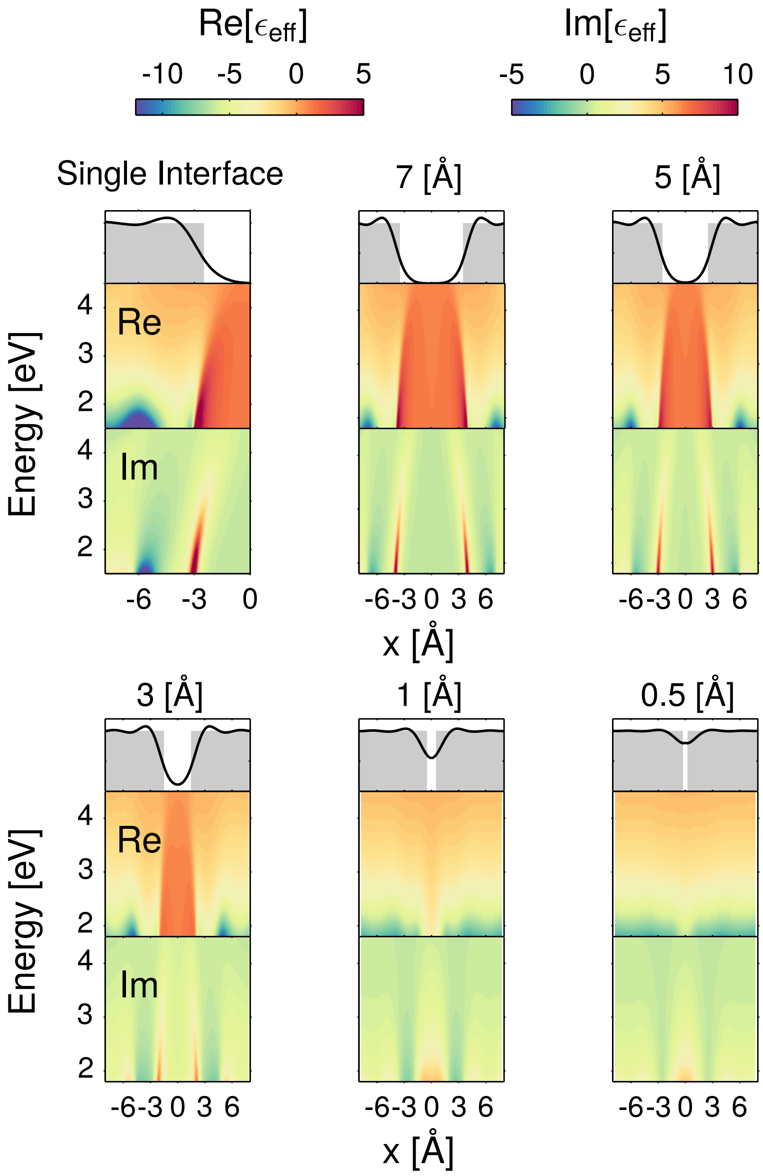

FIG. 12 Effective permittivity of Sodium-vacuum-Sodium structure predicted by the TDDFT for different gap distances.

8.2. Gap Permittivity

Based on the spatial information provided by the TDDFT calculations, we define the effective local permittivity $\epsilon_{\text{eff}}(\mathbf{r})$ by $\epsilon_{\text{eff}}(\mathbf{r}) = \text{D}(\mathbf{r})/[\epsilon_0\text{E}(\mathbf{r})]$. In Fig. 12, ϵ_{eff} for different gap distances are plotted. The TDDFT extracted mid-gap permittivity ϵ_{gap} for gap distances from 5 to 0.5 Å are demonstrated in Fig. 13. The non Drude–Drude transition are clearly observed as the gap is decreasing. For the gap distances of 1Å and 0.5Å, we cast the ϵ_{gap} into the Drude form, and extract the damping rate. It is found that the damping rate decreases as the frequency is increases, and also the 0.5Å gap case has a smaller damping rate.

8.3. Projected-Dipole Gap Model

Treating the gap as an effective medium with permittivity from the TDDFT calculations of a planar dimer in sprit close to the QCM, and also including the single interface quantum effects by the PDM, the proposed model is referred to as a Projected-Dipole Gap Model (PDGM). To illustrate the validity of

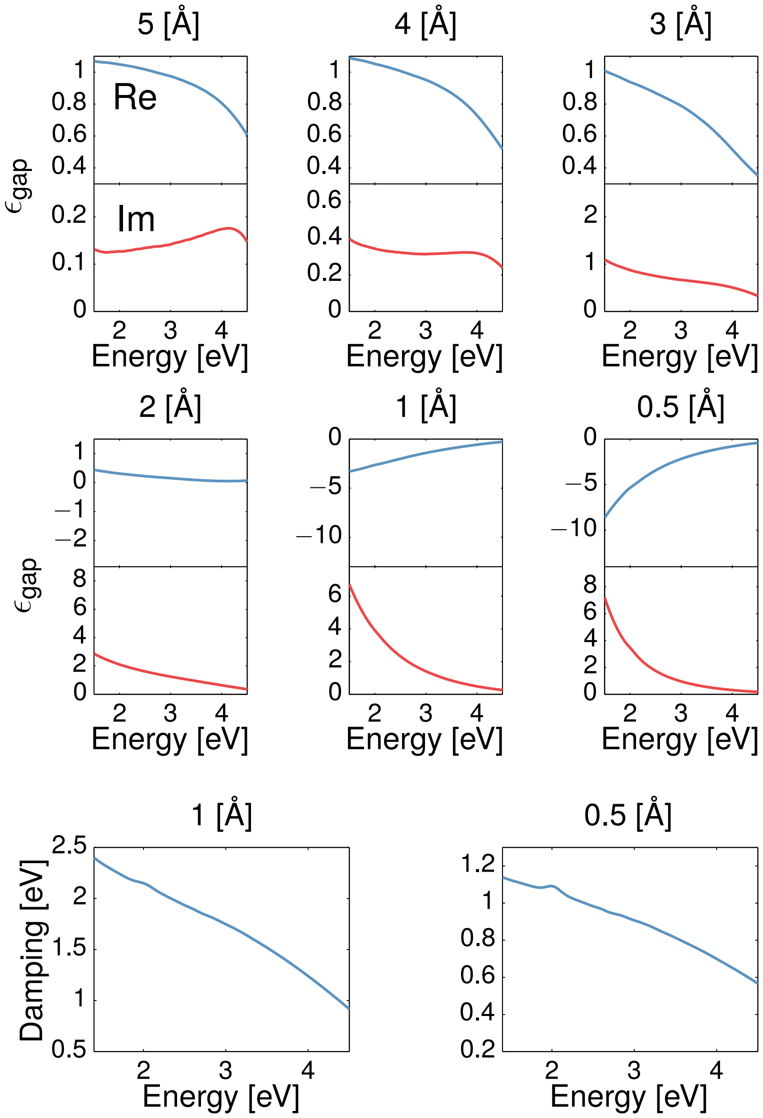

FIG. 13 Effective mid-gap permittivity of Sodium-vacuum-Sodium structure predicted by the TDDFT for gap distances decreasing from 5 Å to 0.5 Å. (b) Damping rate of the gap permittivity predicted by the TDDFT and QCM for gap distances 1 Å and 0.5 Å.

the PDGM, the planar Sodium dimer is investigated. The evolution of the (charge) anti-symmetric gap plasmon resonance energy and its width as a function of the gap distance for the wavenumbers $0.1k_{\mathrm{F}}$ and $0.1k_{\mathrm{F}}$ is plotted in Fig. 14. Overall, the plasmon energy redshifts and the resonance broadens as the gap is reduced. The main observations are: (1) for gaps above 6 Å, the results predicted by the PDGM PDM, and the TDDFT coincide; (2) for gaps below 6 Å, the PDGM and TDDFT are in mutual good agreement, while the simple PDM does handle the emerging wavefunction overlap appropriately; (3) when the separation is below 2Å (grey-shaded region), the plasmon mode continues to exist within the PDM (this being an artifact of the independent-surface approximation), while it is short circuited by a Drude-like conductive current inside the gap region, as predicted by TDDFT and correctly captured by PDGM.

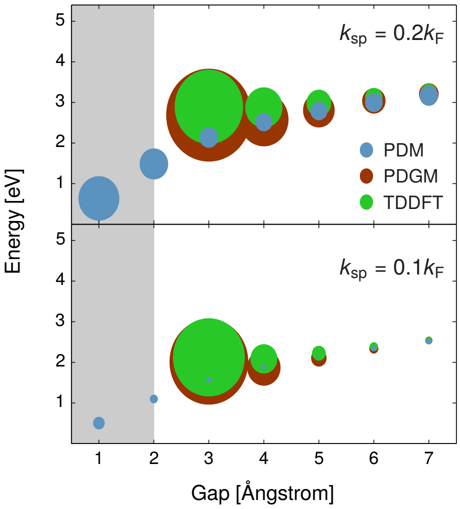

FIG. 14 Dependence of gap plasmon modes on gap distances for plasmon wavenumbers k_{sp} being $0.1k_{\mathrm{F}}$ and $0.2k_{\mathrm{F}}$, calculated by TDDFT, PDM, and also PDGM. The center of data symbols represents the resonance energy, while the size reflects the resonance width.

9. NEAR-FIELD PROPERTIES

In this section, we discuss the performance of the PDM and also the PDGM for predicting the near-field properties of the plasmonic structures. For illustrations, we consider the Sodium cylindrical dimer with radius 4.9 nm and gap distance varying from 1 Å to 10 Å. The incident electric field is along the gap. We plot the field enhancement (FE) at the gap center contrasting LRA, PDM, and PDGM results in Fig. 15. Clearly, the LRA completely fails to predict the FE due to the neglect of the quantum effects. The PDM and PDGM both exhibit the saturation of the FE, even though the PDM slightly overestimates the FE for the gap distance below 5 Å owing to the neglect of the gap dynamics as discussed in Section 8. Comparing with the TDDFT results as presented in Fig. 5 of Ref. 14, we see that the PDGM and TDDFT are in almost perfect agreement, while the PDM and TDDFT agree for gap distances larger than 5 Å where the gap is vacuum like.

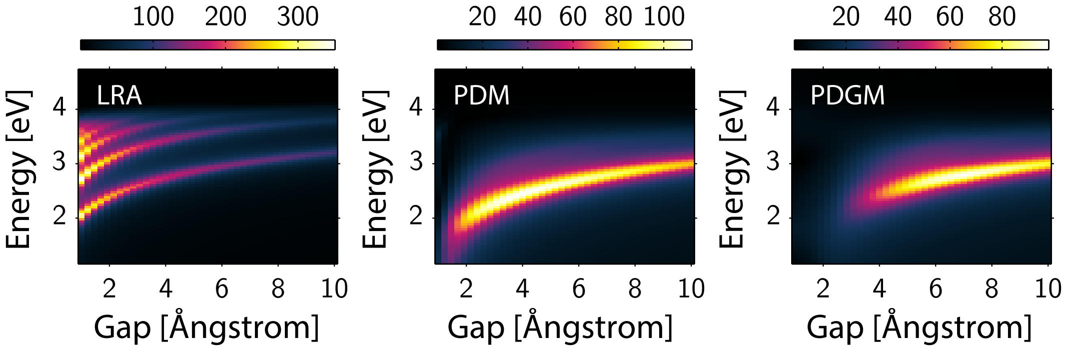

FIG. 15 Field enhancement of the Sodium cylindrical nanowire with radius 4.9 nm and gap distance varying from 1 Å to 10 Å. The incident electric field is along the gap. The LRA, PDM, and PDGM results are illustrated.

References

[1] *Time-Dependent Density Functional Theory* (Springer, Berlin, 2006) lecture Notes in Physics Vol. 706, edited by M. A. L. Marques, C. A. Ullrich, F. Nogueira, A. Rubio, K. Burke, and E. K. U. Gross.

[2] N. Lang and W. Kohn, Phys. Rev. B **12**, 4555 (1970).

[3] U. Leonhardt and T. G. Philbin, Prog. Opt. **53**, 69 (2009).

[4] R. Kimmel and J. A. Stehian, Proc. of National Academy of Sci. **15**, 8431 (1998).

[5] W. Yan, N. A. Mortensen, and M. Wubs, Phys. Rev. B **88**, 155414 (2013).

[6] F. J. García de Abajo and A. Howie, Phys. Rev. Lett. **80**, 5180 (1998).

[7] N. A. Mortensen, S. Raza, M. Wubs, T. Sondergaard, and S. I. Bozhevolnyi, Nat. Commun. **5**, 3809 (2014).

[8] T. V. Teperik, P. Nordlander, J. Aizpurua, and A. G. Borisov, Phys. Rev. Lett. **110**, 263901 (2013).

[9] L. Stella, P. Zhang, F. García-Vidal, A. Rubio, and P. García-González, J. Phys. Chem. C **117**, 8941 (2013).

[10] S. Raza, N. Stenger, S. Kadkhodazadeh, S. V. Fischer, N. Kostesha, A.-P. Jauho, A. Burrows, M. Wubs, and N. A. Mortensen, Nanophotonics **2**, 131 (2013).

[11] C. Ciracì, R. T. Hill, J. J. Mock, Y. Urzhumov, A. I. Fernández-Domínguez, S. A. Maier, J. B. Pendry, A. Chilkoti, and D. R. Smith, Science **337**, 1072 (2012).

[12] R. Esteban, A. Borisov, P. Nordlander, and J. Aizpurua, Nat. Commun. **3**, 825 (2012).

[13] H. Bruus and K. Flensberg, *Many-body Quantum Theory in Condensed Matter Physics: An Introduction* (Oxford University Press, Oxford, 2004).

[14] T. V. Teperik, P. Nordlander, J. Aizpurua, and A. G. Borisov, Opt. Express **21**, 27306 (2013).